

Magnetic-field-induced FM-AFM metamagnetic transition and strong negative magnetoresistance in $\text{Mn}_{1/4}\text{NbS}_2$ under pressure.

S. Polesya,¹ S. Mankovsky,¹ P. G. Naumov,^{2,3} M. A. ElGhazali,² W. Schnelle,² S. Medvedev,² S. Mangelsen,⁴ W. Bensch,⁴ and H. Ebert¹

¹*Department Chemie, Physikalische Chemie, Universität München, Butenandstr. 5-13, 81377 München, Germany*

²*Max Planck Institute for Chemical Physics of Solids,
Nöthnitzer Str. 40, D-01187 Dresden, Germany*

³*Shubnikov Institute of Crystallography, Russian Academy of Sciences, Moscow 119333, Russia*

⁴*Inst. für Anorgan. Chemie, Universität Kiel, Olshausenstr. 40, 24098 Kiel, Germany*

(Dated: March 27, 2020)

Transition metal dichalcogenides (TMDC) stand out with their high chemical stability and the possibility to incorporate a wide range of magnetic species between the layers. The behavior of conduction electrons in such materials intercalated by 3d-elements is closely related to their magnetic properties and can be sensitively controlled by external magnetic fields. Here, we study the magnetotransport properties of NbS_2 intercalated with Mn, $\text{Mn}_{1/4}\text{NbS}_2$, demonstrating a complex behavior of the magnetoresistance and of the ordinary and anomalous Hall resistivities. Application of pressure as tuning parameter leads to the drastic changes of the magnetotransport properties of $\text{Mn}_{1/4}\text{NbS}_2$ exhibiting large negative magnetoresistance up to 65% at 7.1 GPa. First-principles electronic structure calculations indicates pressure-induced transition from ferromagnetic to antiferromagnetic state. Theoretical calculations accounting for the finite temperature magnetic properties of $\text{Mn}_{1/4}\text{NbS}_2$ suggest a field-induced metamagnetic ferromagnetic-antiferromagnetic transition as an origin of the large negative magnetoresistance. These results inspire the development of materials for spintronic applications based on intercalated TMDC with a well controllable metamagnetic transition.

PACS numbers: Valid PACS appear here

I. INTRODUCTION

The transition metal dichalcogenides (TMDC) are in focus of various investigations since many years as they exhibit a broad spectrum of structure and composition dependent physical properties. Being non-magnetic itself, some of the known TMDC materials allow intercalation by magnetic 3d elements¹, having a tendency to the formation of ordered compounds when the concentration of intercalating elements is close to 25% or 33%. This creates a family of TMDC-based magnetic compounds exhibiting rather peculiar magnetic and transport properties, which however have not been well investigated so far. Among the properties of the intercalated TMDC's one can mention the high magnetic anisotropy^{2,3} and anomalous Hall effect (AHE)^{2,4} in $\text{Fe}_{1/4}\text{TaS}_2$ observed experimentally and discussed recently on the basis of the first-principles calculations^{5,6}. A large magnetoresistance (MR) has been found in disordered Fe_xTaS_2 single crystals, up to 60% at $x = 0.28$ ⁷ and 140% at $x = 0.29$ ⁸, that was attributed to the spin disorder and strong spin-orbit coupling in the system. A long-period helimagnetic (HM) structure along the hexagonal c-axis has been observed experimentally in $\text{Cr}_{1/3}\text{NbS}_2$, with the Cr magnetic moments aligned within the basal plane perpendicular to the c-axis^{9,10}. Stabilization of the HM structure in $\text{Cr}_{1/3}\text{NbS}_2$ has been confirmed theoretically by means of first principles calculations¹¹. Similar to $\text{Cr}_{1/3}\text{NbS}_2$ helimagnetic properties have been also predicted for $\text{Mn}_{1/3}\text{NbS}_2$ ¹¹, while for $\text{Fe}_{1/3}\text{NbS}_2$ stabil-

ity of the magnetic structure referred to as an ordering of the third kind was demonstrated¹¹ in agreement with experimental results¹²⁻¹⁴. The calculations demonstrate a transition to the AFM state also for $\text{Co}_{1/3}\text{NbS}_2$ and $\text{Ni}_{1/3}\text{NbS}_2$ ¹⁵, again in line with experiment¹⁶.

Application of pressure provides an appealing degree of freedom to manipulate the physical properties of solids, albeit only a few studies on the 3d-intercalated TMDC materials have been done so far. The pressure induced electronic structure modification can have either a direct impact on the physical properties or can lead first of all to a crystal structure transformations (see e.g.^{17,18}). As a direct impact one can mention the pressure induced changes of the magnetic and transport properties of $\text{Co}_{1/3}\text{NbS}_2$ ¹⁹ as well as an enhancement of the superconducting properties of Fe_xNbS_2 ²⁰ reported recently. On the other hand, a suppression of the helimagnetic structure has been observed for $\text{Cr}_{1/3}\text{NbS}_2$ at $\sim 3 - 4$ GPa as a result of the structural transformations in the system¹⁸.

In the present work we focus on the magnetic properties of Mn intercalated 2H-NbS_2 under pressure, with 25% intercalation concentration. In the first part we discuss the experimental results based on the magnetotransport measurements (magnetoresistance and Hall effect), as they are crucial for inferring information about the interactions between itinerant charge carriers and the magnetic degrees of freedom in a variety of magnetic materials. In order to interpret the details of the experimental measurements, theoretical results are discussed in the

second part, which are based on DFT calculations and Monte Carlo simulations.

II. TECHNICAL DETAILS

A. Experimental details

1. Sample preparation

A mixture of 1 g in total of the elements (Mn, 99.95 %, Alfa Aesar; Nb, 99.9 % chempur; S, 99.9995 %, Alfa Aesar) with nominal stoichiometry $\text{Mn}_{0.265}\text{NbS}_2$ were ground and loaded into an argon flushed silica ampoule. CBr_4 (~ 25 mg, 98 %, Fluka) was added as transport agent. Due to the volatility of CBr_4 the lower end of the filled ampoule was cooled with liquid nitrogen prior to evacuation ($p \leq 1 \times 10^{-4}$ mbar), after which the ampoule was sealed. The ampoule was placed in the natural gradient of a single tube furnace in inverse position for the pre reaction and cleaning transport. After heating to 450°C during 6 h, the temperature was maintained there for 10 h before it was raised to 900°C . After two days the ampoule was placed in a gradient $900^\circ\text{C} \rightarrow \sim 800^\circ\text{C}$ and within 14 d crystals of several mm diameter in the basal plane grew. The ampoule was post-annealed by slow cooling from 800°C to room temperature within 24 h to allow for a good order of the Mn-ions which become disordered above $\sim 400^\circ\text{C}$.^{21–23} After opening the ampoules the crystals were washed with water, a dilute solution of $\text{Na}_2\text{S}_2\text{O}_3$ (97 %, Grüssing), water and acetone. The crystals have dimensions up to several mm in diameter and 1 mm in height and show a metallic silver luster. They were stored in an evacuated desiccator until usage.

2. Characterisation

EDX-spectra were acquired on a Philips XL30 ESEM equipped with an EDAX EDX-detector operated at 20 kV acceleration voltage. At least two crystals from each batch were analysed, on each crystal the composition was measured on three spots with an integration time of 120 s each.

The series of 00l-reflections were measured on a Panalytical X'Pert Pro-MPD (Cu-K_α radiation, $1/16^\circ$ divergence mask, Göbel mirror, primary soller slit (0.04 rad) on the incident beam path, parallel plate collimator and PIXcel 1D detector on the diffracted beam path) in Bragg-Brentano geometry. For sample alignment and rocking curves a receiving slit was used.

For collecting diffraction patterns in [001]-orientation a thin slice ($\leq 100 \mu\text{m}$) was cut from a crystal with a thin razor blade. The crystal piece was mounted on an adhesive tape and measured in transmission geometry on a Panalytical Empyrean diffractometer (Cu-K_α radiation, $1/2^\circ$ divergence mask, focussing mirror, primary soller slit (0.04 rad) on the incident beam path, secondary soller slit

(0.04 rad) and PIXcel 1D detector on the diffracted beam path). The instrumental broadening was derived from a measurement of LaB_6 (NIST SRM 660c) via fitting the profile to a Thompson-Cox-Hastings Pseudo-Voigt profile with a Pawley-fit.

All fittings of the lattice parameters were carried out using Topas-Academic Version 6.0²⁴ via Pawley-fits.

3. Ambient pressure experiments

The magnetization was measured with a MPMS3 (SQUID-VSM, Quantum Design) on a single crystal ($m = 1.859$ mg; flat platelet showing hexagon faces) with the magnetic field applied along the [1000] (in-plane (IP)) or along the [0001] (out-of-plane (OP)) direction, respectively. $M(B)$ isotherms at selected temperatures were recorded after cooling in zero field from $T = 200$ K, temperature sweeps were taken during cooling in low fields. The heat capacity was determined on the same crystal with the HC option in a PPMS-9 (Quantum Design) at zero field and with $B = 9$ T applied along [0001] (OP).

Transverse magnetoresistance (TMR) and Hall resistance ρ_H data as function of magnetic field along [0001] (OP) were measured in a conventional four-wire and a five-wire (with external potentiometer) configuration, respectively. The electrical transport option of a PPMS-9 was used to take data in magnetic field sweeps at selected constant temperatures. Symmetrization of the TMR and antisymmetrization of the Hall data with respect to applied field was performed.

4. High pressure experiments

For high-pressure experiments, a diamond anvil cell manufactured from the nonmagnetic alloy MP35N and equipped with Boehler-Almax design diamond anvils with $500\text{-}\mu\text{m}$ culets was used. The tungsten gasket was insulated with a cubic BN/epoxy mixture. A single crystal sample of suitable size ($120 \mu\text{m} \times 120 \mu\text{m} \times 10 \mu\text{m}$) was cut and placed into the central hole of the gasket filled with NaCl as a pressure-transmitting medium along with a ruby chip for pressure calibration. The electrical leads were fabricated from $5 \mu\text{m}$ thick Pt foil and attached to the sample in a van der Pauw configuration. Electrical resistivity was measured at different pressures in temperature range 1.8–300 K in magnetic field up to 9 T with Physical Property Measurement System (PPMS-9, Quantum Design).

High pressure Raman spectra were recorded at room temperature using a customary confocal micro-Raman spectrometer with a HeNe-laser as the excitation source and a single-grating spectrograph with 1 cm^{-1} resolution. Pressure was measured with accuracy of ~ 0.1 GPa using the ruby luminescence method.

B. Computational details

The first-principles electronic structure calculations have been performed using the spin-polarized relativistic KKR (SPR-KKR) Green function method^{25,26}. For the angular momentum expansion of the Green function a cutoff of $l_{max} = 3$ was applied. All calculations have been performed within the framework of the local spin density approximation (LSDA) to density functional theory (DFT) as well as beyond the level of LSDA by accounting for correlation effects by means of the LDA+U scheme^{27,28}. The LSDA calculations used a parametrization for the exchange and correlation potential as given by Vosko *et al.*²⁹. In the LDA+U calculations the so-called atomic limit expression was used for double-counting correction in the LDA+U functional, with the parameters $U = 3$ eV and $J = 0.7$ eV.

In order to investigate the equilibrium magnetic structure as well as finite temperature magnetic properties of the compounds under consideration, Monte Carlo simulations have been performed, which are based on the Heisenberg model with the exchange coupling parameters J_{ij} calculated from first principles³⁰.

The temperature-dependent behavior of electronic resistivity of the systems under consideration was investigated on the basis of the Kubo-Středa formalism in combination with the alloy analogy model. It allows to account for thermal lattice vibrations³¹ as well as spin fluctuations³² treating them within the adiabatic approximation³³.

The properties corresponding to ambient pressure have been calculated using the structure parameters obtained in experiment. The Mn intercalated TMDC system under investigation, $Mn_{1/4}NbS_2$, exhibits a 2×2 superstructure in the Mn layers arranged within the so-called van der Waals gap, leading to a well defined ordered compound crystallizing in the space group $P6_3/mmc$ (SG194), with $a = 6.67\text{\AA}$, $c = 12.49\text{\AA}$. This implies an occupation of the $(2a)$ Wyckoff positions by Mn atoms, and occupation of the $(2b)$ and $(6h)$ (with $x = 0.5$) positions by Nb atoms, and $(4f)$ - ($z = 0.121$) and $(12k)$ -positions ($x = 5/6, z = 0.37$) – by S atoms.

In the investigations of the pressure dependent properties, the pressure dependent structure parameters of $Mn_{1/4}NbS_2$ have not been measured. Therefore, auxiliary calculations have been performed using the VASP package^{34,35} in order to determine the relationship between the applied pressure and lattice parameters. In these calculations using the GGA density functional for the exchange and correlation potential the PBE-parametrization scheme has been used as given by Perdew *et al.*³⁶. As the van der Waals interactions may be important to describe correctly the pressure dependent behaviour of TMDC-based system³⁷, these interactions have been taken into account using the DFT-D3 method for the dispersion corrections as given by Grimme *et al.*³⁸. The Monkhorst-Pack ($8 \times 8 \times 8$) k -point grid was used for the integration over the Brillouin zone. A plane

wave basis set up to a cutoff energy of 440 eV was used for the wave function representation.

III. RESULTS

A. Experiment

The details of sample preparation are described in section II A. The elemental composition was determined by means of EDX to be $Mn_{0.25}NbS_2$ within the limits of experimental accuracy. The Mn ions are known to form a superstructure of $2a \times 2a$ with respect to the $2H-NbS_2$ host lattice. In fact, the composition determined is very close to the ideal value for this type of superstructure. To check this, X-ray diffraction was carried out on a thin piece cut from a crystal, which was oriented with reflections of the $[001]$ zone axis being under diffraction condition. The corresponding diffraction pattern is presented in Fig. 1 (a). There are only reflections of type $h00$ and $hk0$ visible which have a very narrow full width at half maximum (FWHM), indicating large coherently diffracting domains. This holds true both for the host structure (110 reflection) as well as for the domains of the superstructure (100 reflection). To further ensure the crystal quality the series of 00l-reflections was measured (see Fig. 1 (b)). Also here a very low FWHM can be observed, indicating a large domain size along the c -axis. The rocking curves measured on the 00l-reflections are of a very low average FWHM (0.06° , an example is shown in the inset of Fig. 1 (b)), underscoring the high quality of the crystals.

From the XRD data presented here we can conclude that only the $2a \times 2a$ type superstructure is formed by the Mn-ions with long range order. This is evidenced by the presence of only one set of 00l-reflections and in particular by the diffraction pattern of the $[001]$ zone axis, where only reflections belonging to this type of superstructure are present. The lattice parameters are $a = b = 6.6715(4) \text{\AA}$ and $c = 12.493163(3) \text{\AA}$, in very good agreement with reports from literature.^{12,39?} These measurements showed reproducible results on several crystals from the same batch. In summary, the samples can be described as nearly perfect $Mn_{1/4}NbS_2$.

The magnetic moment of $Mn_{1/4}NbS_2$ as function of the magnetic field $M(H)$ ($\mu_B/\text{f.u.}$) is shown in Fig. 2 for different temperatures. All $M(H)$ curves do not exhibit detectable signature of a field hysteresis. The shape of the magnetization curves shown in Fig. 2 evidence that $Mn_{1/4}NbS_2$ is a soft easy-plane ferromagnet. For both orientations of the magnetic field, in-plane (IP) and out-of-plane (OP), a saturation magnetization at $T = 2.0$ K of $1.05\mu_B/\text{f.u.}$ is attained, indicating a local magnetic moment $M_{Mn} = 4.2\mu_B$ per Mn ion. The observed behavior and the derived characteristic values are in fair agreement with a previous investigation by Onuki *et al.*⁴⁰. Magnetization data measured while cooling or warming in low magnetic fields indicate a ferromagnetic (FM) or-

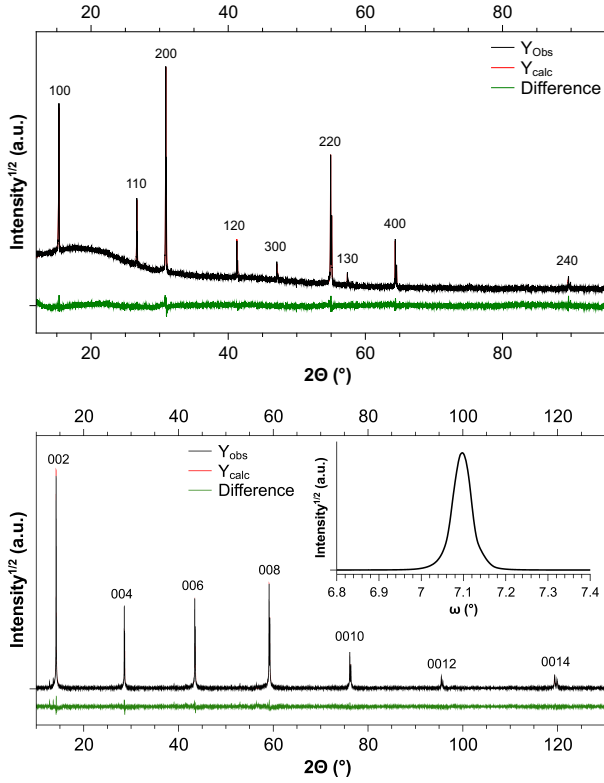
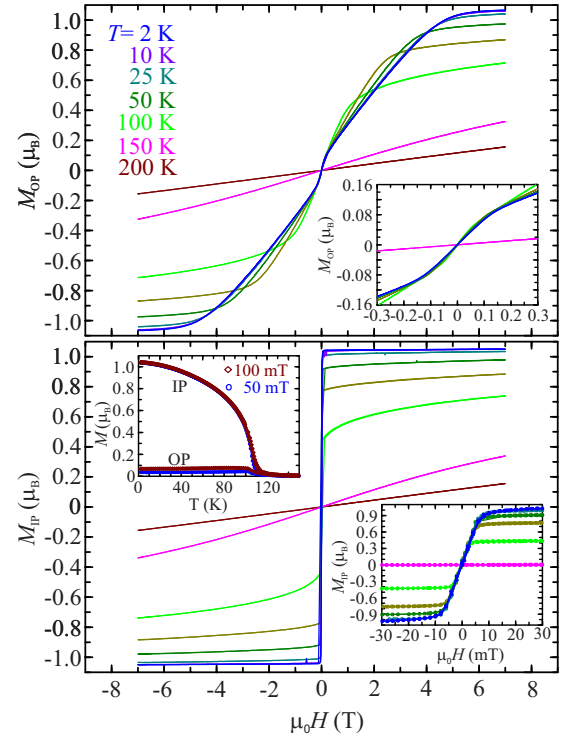


FIG. 1. Observed and calculated diffraction patterns for a sample of $\text{Mn}_{0.25}\text{NbS}_2$ for the set of $hk0$ -reflections (a) and $00l$ -reflections (b). In the inset of (b) a representative rocking curve of the 002 reflection is presented.

dering at $T_C = 104(2)$ K. The same critical temperature is obtained from the heat capacity measurements (SM, Fig. 1).

The electrical resistivity $\rho(T)$ of $\text{Mn}_{1/4}\text{NbS}_2$ (see Fig. 3) measured at different pressure exhibits well defined metallic-like behaviour typical for magnetically ordered systems. For all pressures it decreases upon sample cooling down from room temperature, changing the slope at the critical temperature T_c corresponding to a transition to a magnetically ordered state. At ambient pressure this corresponds to a Curie temperature $T_C \approx 104$ K as $\text{Mn}_{1/4}\text{NbS}_2$ exhibits FM order at lower temperatures. A pressure increase up to 10 GPa results in a continuous decrease of the critical temperature down to ~ 75 K at 10 GPa. However, it increases abruptly to ~ 135 K at 13.5 GPa, while a further pressure increase results in a decrease of the critical temperature reaching 40 K at a pressure of 22.2 GPa; the highest pressure attained in this study.

The sudden increase of the critical temperature at 13.5 GPa can indicate a change of the crystal structure of $\text{Mn}_{1/4}\text{NbS}_2$ above 10 GPa. To monitor the possible structural phase transition, the investigation of the Raman spectra changes for $\text{Mn}_{1/4}\text{NbS}_2$ under pressure have been performed, as is shown in Fig. 4(a). The Raman spectra at ambient pressure are qualitatively



(b) FIG. 2. Magnetic moment M ($\mu_B/\text{f.u.}$) of $\text{Mn}_{1/4}\text{NbS}_2$ as function of the magnetic field oriented along $[0001]$ (a) and along $[1000]$ directions. The inset in (a) displays the magnetic moment as function of temperature, obtained during cooling in low fields of 50 (squares) and 100 mT (diamonds) for both the IP and OP field directions.

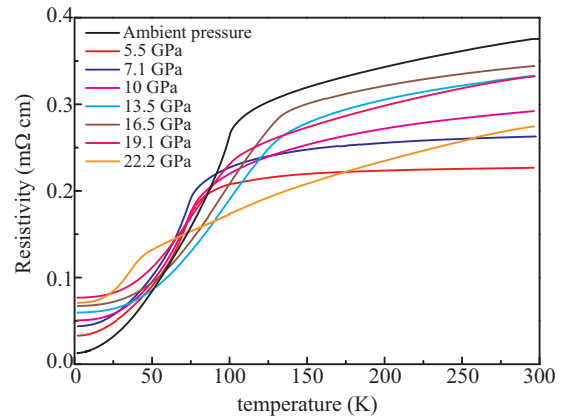


FIG. 3. Electrical resistivity obtained experimentally for $\text{Mn}_{1/4}\text{NbS}_2$ at zero magnetic field, plotted as function of temperature for different pressure values.

similar to that of the related isostructural compound $\text{Fe}_{0.239}\text{NbS}_2$ ⁴¹. All Raman resonances observed at ambient pressure are persistent in the Raman spectra up to the pressures beyond 20 GPa (Fig. 4(a)) while the frequency of these peaks shown in Fig. 4(b) shows normal increase with pressure without any discontinuities indicating no structural phase transition in this pressure

regime. These observations allow to make conclusions about possible changes of the low-temperature magnetic structure of $\text{Mn}_{1/4}\text{NbS}_2$ above 10 GPa. However, we will focus below on the pressure effect in the region up to ~ 10 GPa, while the results obtained at higher pressure need more detailed investigations.

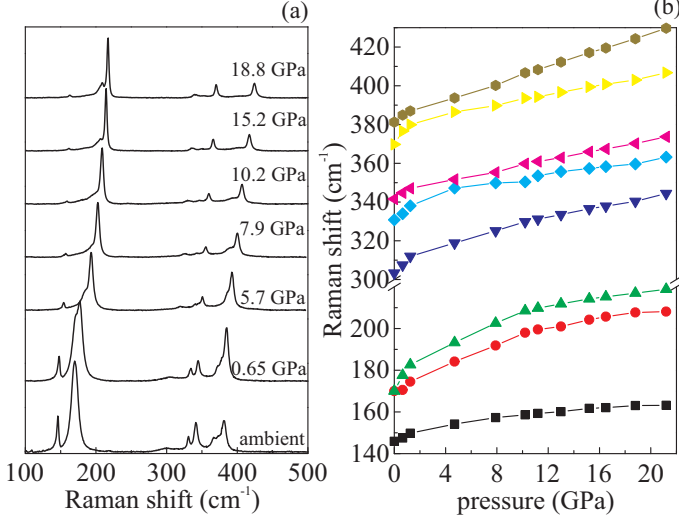


FIG. 4. Pressure evolution of Raman spectra (a) and pressure dependence of the frequencies of the observed Raman peaks (b)

The transverse MR, which is defined as $\text{MR}(\%) = (\rho(T, H) - \rho(T, 0)) / \rho(T, 0) \cdot 100\%$, and the Hall resistance $\rho_H(H)$ measured at ambient pressure are presented in Fig. 5 as a function of applied field H . The MR for the FM state at $T < 10$ K is positive in the magnetic field regime $\mu_0 H \approx 1.5$ to 3.5 T. This behavior is obviously connected to the slow turning of the magnetic moments out-of-plane with increasing field, before reaching magnetic saturation. However, the MR effect is getting negative at higher magnetic field with the maximum at the saturation point. The MR is negative for all magnetic fields when the temperature increases approach T_C , showing a maximum at the Curie temperature. The positive slope for the Hall resistivity (see Fig. 5 (b)) indicates a dominating hole-type conductivity in $\text{Mn}_{1/4}\text{NbS}_2$ at ambient pressure. While linear at high temperatures, the Hall resistivity $\rho_H(H)$ below T_C has a contribution due to the anomalous Hall effect vanishing in the magnetically disordered state.

The magnetoresistance and Hall resistivity measured in the DAC at the lowest applied pressure 0.25 GPa (SM, Fig. 2 (b)) demonstrate qualitatively a similar behaviour compared to ambient pressure. However, application of a higher pressure has a significant impact on the shape of the Hall resistance $\rho_H(H)$ and magnetoresistance $\text{MR}(H)$. The low-temperature magnetotransport data (Fig. 6, as well as Figs. 2 (b), (d), (f), (h) in SM) indicate the pressure-induced change of the MR that can be associated with the modification of magnetic properties

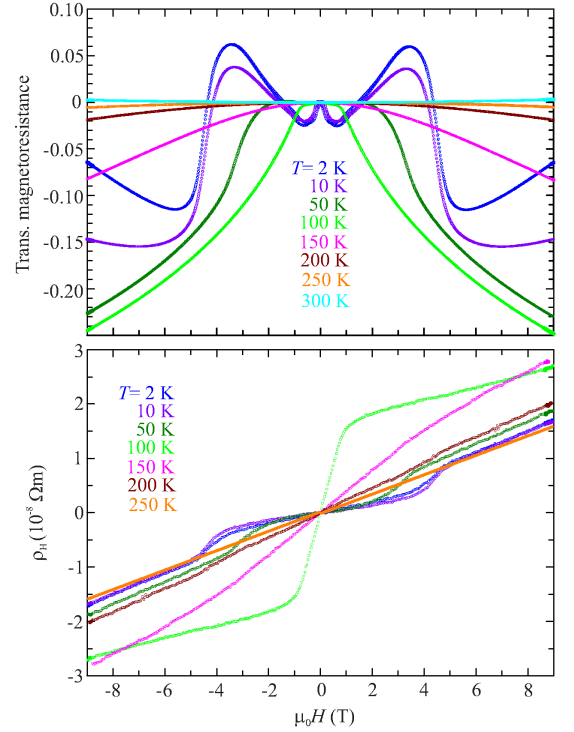


FIG. 5. Transverse magnetoresistance $\text{MR}(T, B)$ (top) and Hall resistance $\rho_H(H)$ (bottom) for $\text{Mn}_{1/4}\text{NbS}_2$ measured at ambient pressure for different temperatures. The magnetic field is applied in the out-of-plane direction.

of $\text{Mn}_{1/4}\text{NbS}_2$. The positive MR observed at ambient pressure is continuously suppressed while the absolute value of the negative MR at the highest fields continuously increases (Fig. 6 (a)). For $p = 5.5$ GPa, MR is negative for all applied magnetic fields, for all temperature regimes (SM, Fig. 2 (d)). Approaching the pressure 7.1 GPa, MR in the high field regime increases up to 65% (Fig. 6(a)). At $p = 10$ GPa, MR drastically drops to 3.2% at 9 T although it remains negative with nearly parabolic dependence. Above 10 GPa, MR suddenly decreases to the very low positive values (only about 0.1% at 9 T at 13.5 GPa).

Hall resistivity curves $\rho_H(H)$ at pressures up to 5.5 GPa at the low temperature (Fig. 6 (b); SM, Fig. 2 (a), (c), (e), (g)) are qualitatively similar to that for ambient pressure demonstrating two regimes. Two regimes in the Hall resistivity curves are still persistent at further pressure increase as can be seen from the $\rho_H(H)$ curve at 7.1 GPa (Fig. 6(b)). At $p = 10$ GPa, Hall resistivity $\rho_H(H)$ is sublinear, while above 10 GPa $\rho_H(H)$ is linear at all temperatures (above and below the critical temperature derived from the temperature dependence of resistivity) with a negative slope revealing dominating electron conductivity in $\text{Mn}_{1/4}\text{NbS}_2$ and $\rho_H(H)$ indicating the suppression of ferromagnetic order. For the magnetically ordered state ($T < T_C$) of $\text{Mn}_{1/4}\text{NbS}_2$, when the temperature increases, one can clearly see the contribution due to the extraordinary Hall effect vanishing in the magnet-

ically disordered state (SM, Fig. 2 (a), (c), (e) and (g)). As it follows from the results for different pressure values ρ_{AHE} changes the sign twice upon pressure increase.

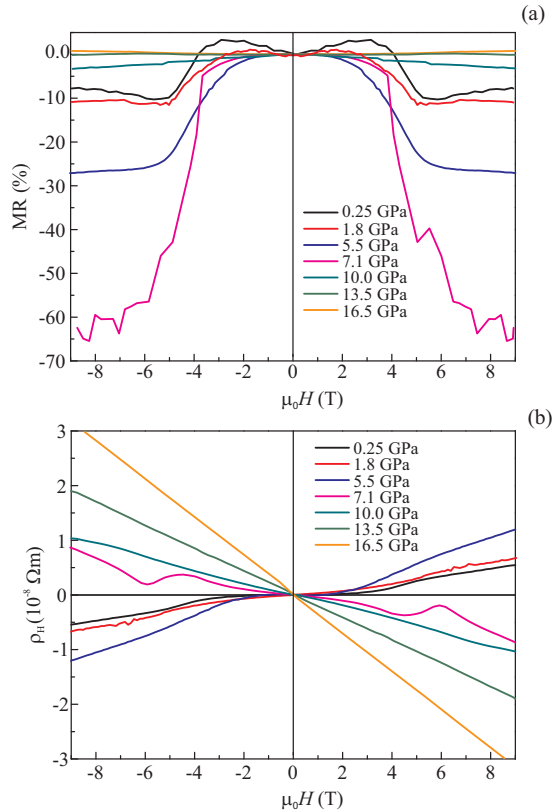


FIG. 6. Pressure and temperature dependent transverse magnetoresistance (a) and Hall resistivity (b) at $T = 2\text{K}$ for $\text{Mn}_{1/4}\text{NbS}_2$ plotted as function of external magnetic field.

B. Theory

To allow a detailed interpretation of the experimental results, theoretical investigations based on first-principles electronic structure calculations have been performed by using the SPR-KKR band structure method^{25,26}. The DFT calculations based on local density approximation (LSDA) for FM $\text{Mn}_{1/4}\text{NbS}_2$ at ambient pressure lead to an underestimation of the Mn spin magnetic moment ($3.3\mu_B$ vs. experimental $4.2\mu_B$ per atom), and to a suppression of the Mn spin magnetic moment at high pressure. Therefore, the calculations have been extended treating correlation effects beyond LSDA, using the LSDA+U approach with the Hubbard U parameter for Mn of $U = 3\text{ eV}$. This leads to an increase of the spin magnetic moment of Mn at ambient pressure up to $3.8\mu_B$ as well as to a stabilization of the finite Mn spin magnetic moment on the Mn atom when the pressure increases up to 11 PGa.

The pressure-volume dependence, $p - V$, determined for ordered $\text{Mn}_{1/4}\text{NbS}_2$ using the VASP package^{34,35} (see

SM, Fig. 3), shows a linear $p - V$ dependence up to a pressure of $\sim 9\text{ GPa}$. At higher pressures one can expect an instability of the original crystalline or magnetic phase. This is in line with the experimental results that show significant changes of the MR when the pressure increases above 10 GPa. On the other hand, the experimental Raman spectra do not exhibit any evidence for a structural phase transition in this pressure regime. As it follows from the electronic structure calculations within the LSDA+U approach, a pressure increase up to $p = 8\text{ GPa}$ leads to a decrease of the Mn spin magnetic moment from $m = 3.8\mu_B$ at ambient pressure down to $m = 3.2\mu_B$ at $p = 8\text{ GPa}$ and to $2.21\mu_B$ at 10.5 GPa. Thus, one may speculate about a possible pressure induced transition to the low-spin magnetic state. However, more detailed investigations on the properties of $\text{Mn}_{1/4}\text{NbS}_2$, both theoretical and experimental, are required for this pressure regime, while we will focus here on the low-pressure phase exhibiting linear $p - V$ dependence shown in Fig. 3 (SM).

The properties of the Hall resistivity are determined by the features of the electronic structure. To demonstrate this, Fig. 7 shows the calculated Bloch spectral functions (BSF) $A(\vec{k}, E)$ ((a) and (b)), and $A(k_{||}, E_F)$ ((c) and (d)) representing the electronic band structure and Fermi surface projection onto the (001) plane for the two pressures $p = 0$ and 8 GPa, respectively. A positive slope of the Hall resistivity $\rho_H(B)$ found experimentally at ambient and small pressures implies a dominating hole type character of the electric carriers in line with the hole-like pockets around the K -point of the BZ (see Fig. 7 (a)) created by the unoccupied top of the minority-spin bands (red symbols). This is also seen in the Fermi surface cut shown in Fig. 7 (c) (right panel) representing the Fermi surface created by the minority-spin states, as well as the hole-like pockets created by the majority-spin states (7 (a) blue symbols) along the $\Gamma - M$ and $K - M$ symmetry directions. When the pressure increases above 3.5 GPa, the minority-spin pockets at the K point disappear as the corresponding energy bands (red) move down in energy, as can be seen in Fig. 7 (b) for $p = 8.0\text{ GPa}$. At this pressure, the shape of the Fermi surface has essentially electron-like features (see Fig. 7(d)), leading to the electron-like character for the ordinary Hall effect, although the hole-like pockets created by the majority-spin states around Γ point still survive also at this pressure.

The MR is a characteristic of the change of the electrical resistivity $\rho(T, B)$ in the presence of an external magnetic field B . The corresponding resistivities $\rho(T, B)$ are calculated for the mono-domain system, as a function of the temperature. Therefore, in the case of FM-ordered $\text{Mn}_{1/4}\text{NbS}_2$, these results should be compared with the experimental data for an applied magnetic field strong enough to ensure magnetization saturation in the system.

The temperature dependent electrical resistivity of magnetically ordered metallic systems is determined by thermally induced lattice vibrations and spin fluctuations. Because of a weak dependence of the lattice vi-

brations on the magnetic field, their contribution to the MR can be neglected and we will focus on the transverse spin fluctuations that are strongly affected by the temperature and dependent on the magnetic structure in the system. Monte Carlo (MC) simulations give access to the $M(T, B)$ dependencies for $\text{Mn}_{1/4}\text{NbS}_2$ characterizing the amplitude of the transverse spin fluctuations and as a result the amplitude of the electron scattering on thermal spin fluctuations. These simulations use the exchange coupling parameters obtained within first-principles calculations performed for the FM reference state. A positive first- and second-neighbor exchange coupling parameters J_{ij} at low pressure (see Fig. 8(a)) guarantee the FM ground state of the system. The $M(T, B)$ dependence obtained within MC simulations for $\text{Mn}_{1/4}\text{NbS}_2$ at ambient pressure is shown in Fig. 8 (b) for $B = 0$ T and 4 T, respectively. The resistivities as a function of the temperature calculated on the basis of $M(T, 0)$ and $M(T, B = 4 \text{ T})$ lead to the negative magnetoresistance $\text{MR}(T)$ plotted in Fig. 9 (b). In this case the MR is governed by the mechanism rather common for FM metals⁴²: alignment of the spin magnetic moments along the magnetic field reduces the electron scattering and decreases the resistivity $\rho(T, B = 4 \text{ T})$ with respect to $\rho(T, 0)$, leading to a negative magnetoresistance in the FM ordered system^{43,44}. The impact of the field on the magnetization has a maximum around the Curie temperature, leading to a maximum of the MR in this temperature region. This is in good agreement with the experimental findings as it is shown in Fig. 9 (a).

When the pressure increases, the calculated exchange coupling parameters J_{ij} exhibit significant changes, as shown in Fig. 8(a). The first-neighbor interaction parameters corresponding to an interaction between the Mn ions located in neighboring Mn layers in $\text{Mn}_{1/4}\text{NbS}_2$ become negative when the pressure is approaching $p = 8$ GPa. This should lead to an antiferromagnetic alignment of the magnetic moments of these layers if no other interactions are taken into account. The second-neighbor parameters characterizing the Mn-Mn interactions within the layers are positive, stabilizing the FM order within the layers, although they decrease with increasing pressure. The total energy calculations for $p = 8$ GPa give the difference $E_{\text{FM}} - E_{\text{AFM}} = 36$ meV per formula unit, indicating stability of the AFM state. The dependence of the exchange coupling parameters on the magnetic configuration can be crucial to describe metamagnetic phase transitions properly as it was found for instance discussing the AFM-FM transition in FeRh ⁴⁵. Therefore, the calculations of J_{ij} for $\text{Mn}_{1/4}\text{NbS}_2$ at $p = 8$ GPa have been performed for the AFM reference state with the layer-by-layer antiferromagnetic alignment of the magnetic moments. The resulting Mn-Mn exchange coupling parameters presented in Fig. 8(a) by closed triangles, stabilize the AFM state in the system. This is shown by MC simulations taking into account the exchange interactions only within a sphere with radius $R = 2a$, with a the lattice parameter (see Fig. 8(c), closed circles). The

external magnetic field pushes the magnetic moments towards the FM alignment (see open circles in Fig. 8 (c)). This leads to a modification of the Mn-Mn exchange interaction parameters (Fig. 8(a), open triangles) and to a stabilization of the FM state. Note that in the case of ambient pressure, the exchange parameters calculated both for the FM as well as for the AFM reference state indicate stability of the FM state (Fig. 8(c), diamonds). Thus, one can expect a field-induced AFM-FM transition at $p = 8$ GPa. MC simulations for the pressure $p = 9$ GPa demonstrate the stability of the layer-by-layer AFM state (see Fig. 8 (d)) for which the field induced metamagnetic transition is not possible anymore (see Fig. 8 (d), open circles).

To discuss the behaviour of the magnetoresistance $\text{MR}(T)$ of $\text{Mn}_{1/4}\text{NbS}_2$ at $p = 8$ GPa, the change of the resistivity during the AFM-to-FM transition was calculated as a difference of the electrical resistivities for the AFM (i.e., without magnetic field) and for the FM (with magnetic field) states of the system. The AFM state was approximated by the layer-by-layer antiferromagnetic structure, i.e. with two sublattices having antiparallel alignment of the magnetic moments. For the sake of simplicity, the temperature dependent magnetization for each sublattice, $M(T)$, was taken the same as for the FM state calculated for $p = 8$ GPa (open diamonds in Fig. 8 (c)). The resulting MR is shown in Fig. 9 (b) by circles as a function of the temperature. A crucial result following from these calculations is the maximum of the MR at low temperature due to weak thermal disorder in the system. When the temperature increases the MR decreases and vanishes at the critical temperature due to a transition to the paramagnetic state. A similar behavior of the MR has been obtained experimentally, as it is shown in Fig. 9 (a) by circles.

Finally, it is worth to discuss briefly also the pressure dependent behavior of the non-conventional contribution to the Hall resistivity for $\text{Mn}_{1/4}\text{NbS}_2$. As it was shown above, the high-field $\rho_H(B)$ extrapolated to the $B = 0$ T limit gives the AH resistivity (AHR) assuming FM order in the system, which exhibits a non-monotonous behaviour changing sign twice upon the pressure increase up to 10 GPa (see SM, Fig. 2 (a), (c), (e)). However, no indication for a sign change of the AHR has been found in calculations for the FM state of the system.

On the other hand, in the intermediate pressure regime, before the layer-by-layer AFM state is stabilized, a non-collinear AFM structure is expected as a results of competition between the FM and AFM interatomic exchange interactions. Moreover, in this case the Dzyaloshinskii-Moriya interactions (DMI) should have a crucial role for the formation of a chiral magnetic texture, despite its magnitude (~ 0.2 meV) is smaller by an order of magnitude when compared to the competing isotropic exchange interactions. As a result, an additional topological contribution to the Hall resistivity occurs in the presence of an external magnetic field, ρ_{xy}^{THE} (topological

Hall effect (THE))⁴⁶

$$\rho_{xy} = \rho_{xy}^{OHE} + \rho_{xy}^{AHE} + \rho_{xy}^{THE} \quad (1)$$

with $\rho_{xy}^{AHE} \sim M_z$ and $\rho_{xy}^{THE} \sim \vec{B}_{eff}$, where M_z is the magnetization component along the z direction and \vec{B}_{eff} is the emergent magnetic field having topological origin and being nonzero in the magnetic textures characterized by finite scalar chirality. Note also that a competition of the DMI with the isotropic exchange interactions and the applied magnetic field can lead also to the formation of more complicated topologically nontrivial magnetic textures (e.g. skyrmions) as it was predicted recently for $\text{Fe}_{1/4}\text{TaS}_2$ ⁴⁵. Both extraordinary contributions to the Hall resistivity increase in the system with the in-plane magnetic anisotropy due to increase of the external magnetic field.

IV. SUMMARY

To summarize, we present the results of experimental and theoretical investigations on the pressure dependent magnetic and transport properties of $\text{Mn}_{1/4}\text{NbS}_2$. A strong increase of the magnetoresistance up to $\sim 60\%$ at low temperature has been observed experimentally for the pressure $p = 7.1$ GPa. To get insight into the driving mechanism behind this phenomenon, theoretical investigations have been performed based on first-principles electronic structure calculations combined with Monte Carlo simulations. As a result, the field-induced metamagnetic AFM-FM transition was suggested as a mechanism responsible for the high magnetoresistance at $p = 7.1$ GPa, which is larger than $\sim 50\%$ as was observed

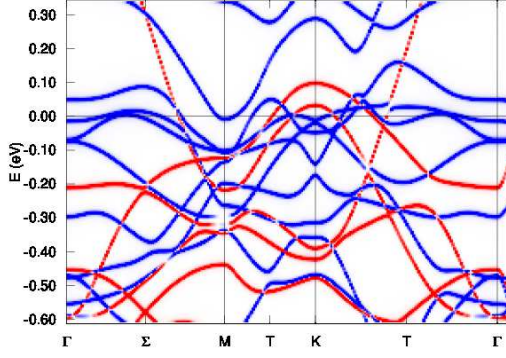
for FeRh ^{47?}. This suggests a new family of materials with controllable metamagnetic transition from AFM to FM ordering that is very promising for various future applications, i.e. materials based on intercalated TMDCs, for which however tuning of the interatomic exchange parameters due to composition variation instead of pressure may be more appropriate. In particular, one can expect a transition from the FM to the AFM state upon substitution of Mn by Fe, coming towards AFM-ordered $\text{Fe}_{1/4}\text{NbS}_2$ ¹³. The pressure induced modification of the Hall resistivity including ordinary and extraordinary (anomalous and topological) contributions is discussed on the basis of calculated electronic structure and exchange coupling parameters and their modifications induced by increasing pressure. Mutual analysis of the experimental and theoretical results allows to make a suggestion about the field-controlled formation of chiral magnetic structure in the intermediate pressure regime characterized by strong competition of the FM and AFM interatomic exchange interactions in $\text{Mn}_{1/4}\text{NbS}_2$.

V. ACKNOWLEDGMENTS

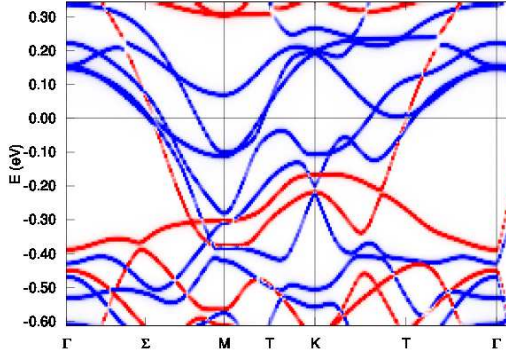
The work in Dresden was supported by the German Research Foundation (DFG) under Projects No. ME 3652/3-1 and GRK 1621 and by the ERC Advanced Grant No. 742068 "TOPMAT". PGN acknowledges the support by the Russian Science Foundation (Project No.17-72-20200). Financial support by the German Research Foundation (DFG) under the project BE 1653/35-1 and by the state of Schleswig Holstein is gratefully acknowledged for the work carried out in Kiel. SP and SM (München) acknowledges a financial support from the DFG via SFB 1277 and via the priority program EB154/36-1.

-
- ¹ R. Friend and A. Yoffe, *Advances in Physics* **36**, 1 (1987), <http://dx.doi.org/10.1080/00018738700101951>.
 - ² J. G. Checkelsky, M. Lee, E. Morosan, R. J. Cava, and N. P. Ong, *Phys. Rev. B* **77**, 014433 (2008).
 - ³ Y. J. Choi, S. B. Kim, T. Asada, S. Park, W. Wu, Y. Horibe, and S.-W. Cheong, *Europhys. Lett.* **86**, 37012 (2009).
 - ⁴ J. Dijkstra, P. J. Zijlema, C. F. van Bruggen, C. Haas, and R. A. de Groot, *Journal of Physics: Condensed Matter* **1**, 6363 (1989).
 - ⁵ K.-T. Ko, K. Kim, S. B. Kim, H.-D. Kim, J.-Y. Kim, B. I. Min, J.-H. Park, F.-H. Chang, H.-J. Lin, A. Tanaka, and S.-W. Cheong, *Phys. Rev. Lett.* **107**, 247201 (2011).
 - ⁶ S. Mankovsky, K. Chadova, D. Ködderitzsch, J. Minář, H. Ebert, and W. Bensch, *Phys. Rev. B* **92**, 144413 (2015).
 - ⁷ W. J. Hardy, C.-W. Chen, A. Marcinkova, H. Ji, J. Sinova, D. Natelson, and E. Morosan, *Phys. Rev. B* **91**, 054426 (2015).
 - ⁸ C.-W. Chen, S. Chikara, V. S. Zapf, and E. Morosan, *Phys. Rev. B* **94**, 054406 (2016).
 - ⁹ Y. Togawa, T. Koyama, K. Takayanagi, S. Mori, Y. Kousaka, J. Akimitsu, S. Nishihara, K. Inoue, A. S. Ovchinnikov, and J. Kishine, *Phys. Rev. Lett.* **108**, 107202 (2012).
 - ¹⁰ D. Braam, C. Gomez, S. Tezok, E. V. L. de Mello, L. Li, D. Mandrus, H.-Y. Kee, and J. E. Sonier, *Phys. Rev. B* **91**, 144407 (2015).
 - ¹¹ S. Mankovsky, S. Polesya, H. Ebert, and W. Bensch, *Phys. Rev. B* **94**, 184430 (2016).
 - ¹² B. V. Laar, H. Rietveld, and D. Ijdo, *J. Solid State Chem.* **3**, 154 (1971).
 - ¹³ O. Gorochoy, A. L. Blanc-soreau, J. Rouxel, P. Imbert, and G. Jehanno, *Phil. Mag. B* **43**, 621 (1981), <http://dx.doi.org/10.1080/01418638108222164>.
 - ¹⁴ Y. Yamamura, S. Moriyama, T. Tsuji, Y. Iwasa, M. Koyano, S. Katayama, and M. Ito, *Journal of Alloys and Compounds* **383**, 338 (2004), proceedings of the 14th International Conference on Solid Compounds of Transition Elements (SCTE 2003).
 - ¹⁵ S. Polesya, S. Mankovsky, and H. Ebert, *Z. Naturf. B* **74**, 91 (2019).
 - ¹⁶ S. S. P. Parkin and R. H. Friend, *Philosophical Magazine Part B* **41**, 65 (1980), <http://dx.doi.org/10.1080/13642818008245370>.

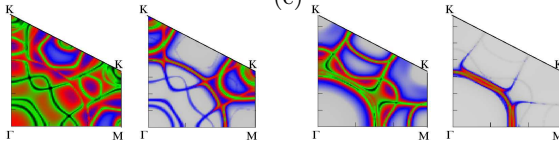
- ¹⁷ L. Ehm, K. Knorr, L. Peters, S. Rath, and W. Depmeier, *J. Alloys Compd.* **429**, 82 (2007).
- ¹⁸ M. Mito, T. Tajiri, K. Tsuruta, H. Deguchi, J. Kishine, K. Inoue, Y. Kousaka, Y. Nakao, and J. Akimitsu, *J. Appl. Phys.* **117**, 183904 (2015).
- ¹⁹ N. Barišić, I. Smiljanić, P. Popčević, A. Bilušić, E. Tutiš, A. Smontara, H. Berger, J. Jaćimović, O. Yuli, and L. Forró, *Phys. Rev. B* **84**, 075157 (2011).
- ²⁰ M. Krishnan, R. Pervin, K. S. Ganesan, K. Murugesan, G. Lingannan, A. K. Verma, P. M. Shirage, and A. Sonachalam, *Sci. Rep.* **8**, 1251 (2018).
- ²¹ F. Boswell, W. Vaughan, and J. Corbett, *J. Solid State Chem.* **24**, 115 (1978).
- ²² Y. Kuroiwa, M. Kunikata, H. Honda, Y. Noda, E. Kita, and A. Tasaki, *J. Phys. Soc. Jpn.* **66**, 1698 (1997).
- ²³ Y. Kuroiwa, M. Kunikata, and Y. Noda, *Mol. Cryst. and Liq. Cryst.* **341**, 87 (2000).
- ²⁴ A. A. Coelho, *J. Appl. Crystallogr.* **51**, 210 (2018).
- ²⁵ H. Ebert et al., *The Munich SPR-KKR package*, version 7.7, <http://olymp.cup.uni-muenchen.de/ak/ebert/SPRKKR> (2017).
- ²⁶ H. Ebert, D. Ködderitzsch, and J. Minár, *Rep. Prog. Phys.* **74**, 096501 (2011).
- ²⁷ A. B. Shick, A. I. Liechtenstein, and W. E. Pickett, *Phys. Rev. B* **60**, 10763 (1999).
- ²⁸ A. N. Yaresko, V. N. Antonov, and P. Fulde, *Phys. Rev. B* **67**, 155103 (2003).
- ²⁹ S. H. Vosko, L. Wilk, and M. Nusair, *Can. J. Phys.* **58**, 1200 (1980), <http://www.nrcresearchpress.com/doi/pdf/10.1139/p80-159>.
- ³⁰ H. Ebert and S. Mankovsky, *Phys. Rev. B* **79**, 045209 (2009).
- ³¹ D. Ködderitzsch, K. Chadova, J. Minár, and H. Ebert, *New Journal of Physics* **15**, 053009 (2013).
- ³² H. Ebert, S. Mankovsky, K. Chadova, S. Polesya, J. Minár, and D. Ködderitzsch, *Phys. Rev. B* **91**, 165132 (2015).
- ³³ V. P. Antropov, M. I. Katsnelson, B. N. Harmon, M. van Schilfgaarde, and D. Kusnezov, *Phys. Rev. B* **54**, 1019 (1996).
- ³⁴ G. Kresse and J. Hafner, *Phys. Rev. B* **47**, 558 (1993).
- ³⁵ G. Kresse and J. Hafner, *Journal of Physics: Condensed Matter* **6**, 8245 (1994).
- ³⁶ J. P. Perdew, K. Burke, and M. Ernzerhof, *Phys. Rev. Lett.* **77**, 3865 (1996).
- ³⁷ S. Mangelsen, P. G. Naumov, O. I. Barkalov, S. A. Medvedev, W. Schnelle, M. Bobnar, S. Mankovsky, S. Polesya, C. Näther, H. Ebert, and W. Bensch, *Phys. Rev. B* **96**, 205148 (2017).
- ³⁸ S. Grimme, J. Antony, S. Ehrlich, and H. Krieg, *J. Chem. Phys.* **132**, 154104 (2010), <https://doi.org/10.1063/1.3382344>.
- ³⁹ A. L. Blanc-Soreau, J. Rouxel, M.-F. Gardette, and O. Gorochoy, *Mater. Res. Bull.* **11**, 1061 (1976).
- ⁴⁰ Y. Onuki, K. Ina, T. Hirai, and T. Komatsubara, *J. Phys. Soc. Japan* **55**, 347 (1986), <https://doi.org/10.1143/JPSJ.55.347>.
- ⁴¹ M. Koyano, H. Watanabe, Y. Yamamura, T. Tsuji, and S. Katayama, *Molecular Crystals and Liquid Crystals Science and Technology. Section A. Molecular Crystals and Liquid Crystals* **341**, 33 (2000), <http://dx.doi.org/10.1080/10587250008026113>.
- ⁴² H. Yamada and S. Takada, *Progress of Theoretical Physics* **48**, 1828 (1972), <http://oup.prod.sis.lan/ptp/article-pdf/48/6/1828/5250340/48-6-1828.pdf>.
- ⁴³ K. Ueda, *Solid State Communications* **19**, 965 (1976).
- ⁴⁴ N. Manyala, Y. Sidis, J. F. DiTusa, G. Aeppli, D. P. Young, and Z. Fisk, *Nature* **404**, 581 (2000).
- ⁴⁵ S. Polesya, S. Mankovsky, D. Ködderitzsch, J. Minár, and H. Ebert, *Phys. Rev. B* **93**, 024423 (2016).
- ⁴⁶ N. Nagaosa, J. Sinova, S. Onoda, A. H. MacDonald, and N. P. Ong, *Rev. Mod. Phys.* **82**, 1539 (2010).
- ⁴⁷ M. A. de Vries, M. Loving, A. P. Mihai, L. H. Lewis, D. Heiman, and C. H. Marrows, *New Journal of Physics* **15**, 013008 (2013).



(a)



(b)



(c)

(d)

FIG. 7. Bloch spectral function for $\text{Mn}_{1/4}\text{NbS}_2$ under pressure for $p = 0$ and 8.0 GPa, (a) and (b), respectively. Blue symbols display majority-spin states and red symbols - minority-spin states. (c) and (d) represent the Bloch spectral function $A(k_x, k_y, E_F)$ at the Fermi level for $\text{Mn}_{1/4}\text{NbS}_2$ under pressure for $p = 0$ and 8.0 GPa, respectively. Left panel corresponds to majority-spin states, right to minority spin states.

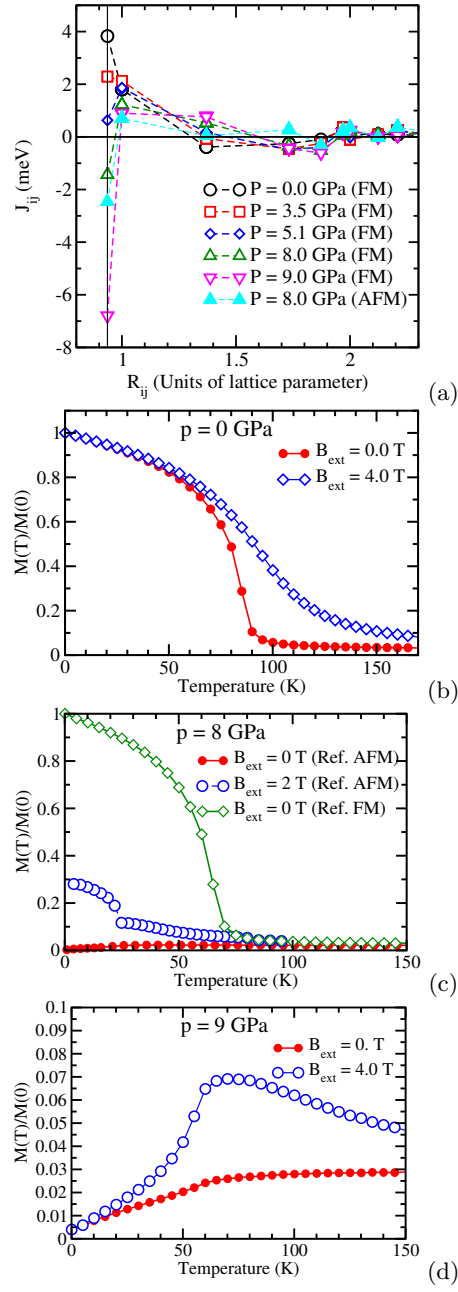


FIG. 8. (a) Pressure dependent exchange interactions for $\text{Mn}_{1/4}\text{NbS}_2$; Open symbols represent the results calculated for the FM reference states, closed symbols the AFM reference state. The MC results for the temperature dependent magnetization $M(T)$ of $\text{Mn}_{1/4}\text{NbS}_2$ for different pressure: $M(T)$ calculated for $B = 0$ (closed circles) and 4.0 T (open circles) at $p = 0.0$ (b), $p = 8.0$ (c) and $p = 9.0$ GPa (d).

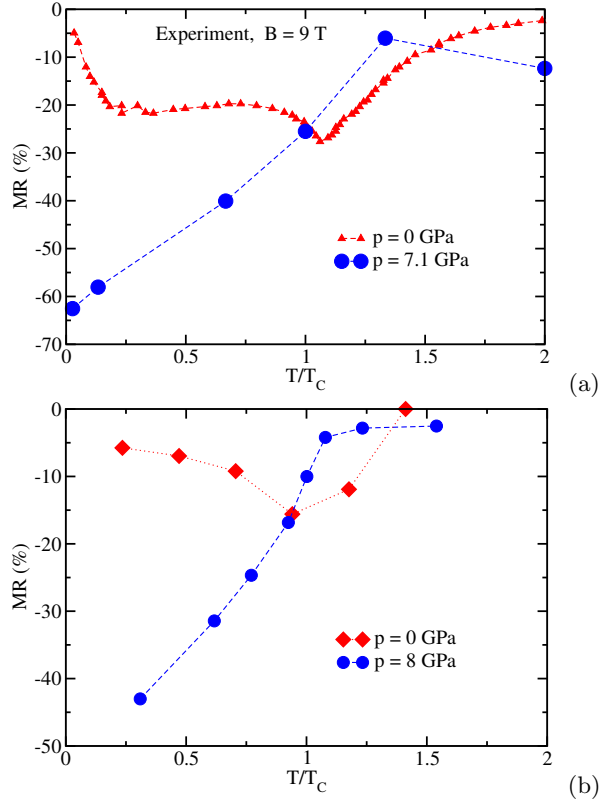


FIG. 9. (a) The temperature dependent magnetoresistance of $\text{Mn}_{1/4}\text{NbS}_2$: (a) Experimental results for the magnetic field $B = 7.5$ T and the two pressures 0 and 7.1 GPa; (b) theoretical results for the magnetic field $B = 4$ T used in the case of $p = 0$ and 5 GPa. The results for $p = 8$ GPa are obtained using the resistivities for the FM and AFM states, $\text{MR} = (\rho(T, \text{FM}) - \rho(T, \text{AFM}))/\rho(T, \text{AFM})$.